University of Kent

Kent Academic Repository

Livens, P., Van der Jeught, S., Dirckx, J. J. J. and Bradu, Adrian (2025) *Frequency-depend assessment of eardrum lesions using multisine OCT vibrometry*. Hearing research, 469 . ISSN 0378-5955.

Downloaded from

https://kar.kent.ac.uk/112337/ The University of Kent's Academic Repository KAR

The version of record is available from

https://doi.org/10.1016/j.heares.2025.109481

This document version

Author's Accepted Manuscript

DOI for this version

Licence for this version

CC BY-NC-ND (Attribution-NonCommercial-NoDerivatives)

Additional information

Versions of research works

Versions of Record

If this version is the version of record, it is the same as the published version available on the publisher's web site. Cite as the published version.

Author Accepted Manuscripts

If this document is identified as the Author Accepted Manuscript it is the version after peer review but before type setting, copy editing or publisher branding. Cite as Surname, Initial. (Year) 'Title of article'. To be published in ***Title of Journal*** , Volume and issue numbers [peer-reviewed accepted version]. Available at: DOI or URL (Accessed: date).

Enquiries

If you have questions about this document contact ResearchSupport@kent.ac.uk. Please include the URL of the record in KAR. If you believe that your, or a third party's rights have been compromised through this document please see our Take Down policy (available from https://www.kent.ac.uk/guides/kar-the-kent-academic-repository#policies).

Frequency-dependent assessment of eardrum lesions using multisine OCT vibrometry

P. Livens[a], S. Van der Jeught[b] , J.J.J. Dirckx[a], A. Bradu[c]

[a]*Bio - & Medical physics lab (BIMEF), University of Antwerp, Department of Physics, Antwerp, Belgium*

[b]*Industrial Vision lab (InViLab), University of Antwerp, Department of Electromechanical Engineering, Antwerp, Belgium*

[c]*Applied Optics Group, School of Electronics, Mathematics and Physics, University of Kent, Canterbury, UK*

Abstract

Optical coherence tomography (OCT) vibrometry is a promising tool for middle-ear mechanics, but single-frequency approaches limit efficiency and diagnostic power. We introduce multisine OCT vibrometry in a rabbit model to capture broadband, frequency-dependent eardrum vibrations acquired in a single OCT volume. Multisine data revealed that control ears had maximal umbo displacement at 1.4 kHz with an amplitude of 86 $\pm$ 11 nm (N=5). Proof-of-concept measurements were performed to highlight the diagnostic value of detecting pathology related shifts in umbo displacement using multisines. Local thinning of the eardrum by ablation decreased the frequency of maximal displacement to 1.0 kHz, and resulted in an umbo displacement of 84 $\pm$ 4 nm. In contrast, perforation of the eardrum caused an overall drop in displacement amplitude across frequencies, with a maximal displacement of 34 $\pm$ 3 nm reached at 2 kHz. Additionally, the single multisine OCT volume allowed visualization of the eardrum's displacement across the surface for all multisine tones. Ablation and perforations caused localized changes of the eardrum's displacement at frequencies above 4 kHz. Thus, multisine OCT vibrometry holds promise for improved diagnosis and surgical planning: umbo frequency-displacement curves can distinguish between healthy and pathological ears, while spatial displacement maps reveal lesion-specific displacement patterns at high frequencies.

Keywords

Optical coherence tomography (OCT); Multisine stimulation; Middle ear mechanics; Diagnostic imaging

Introduction

Disorders of the middle ear and the resulting conductive hearing loss remain a frequent reason for clinical consultation and surgical intervention. Current clinical assessments such as tympanometry and pure-tone audiometry provide useful measures of middle-ear function but can yield ambiguous results in cases with complex pathology (Sanford et al., 2023). Tympanometry, for example, provides a tone stimulus in the ear canal, and uses the amount of reflected sound by the tympanic membrane (TM) as a proxy for middle ear dysfunction. Since tympanometry only measures the total back-reflected sound, it cannot accurately determine the location and size of a TM perforation. However, experimental work has shown that the location, size, and orientation of a perforation significantly influences the resulting conductive hearing loss (Bevis et al., 2022; O'Connor et al., 2008).

Currently, no clinical technique provides information on both morphology and middle ear frequency response, requiring patients to undergo a series of multimodal tests.

Optical coherence tomography (OCT) has recently emerged as a powerful imaging modality for otologic applications (Burkhardt et al., 2014; Liu et al., 2024; Lui et al., 2021; MacDougall et al., 2019), since it can deliver micrometer-scale structural images and acquire nanometer-scale motion of middle-ear structures (Chang et al., 2013; Park et al., 2018; Ramier et al., 2018). Hand-held OCT systems have demonstrated feasibility for in-vivo TM imaging and functional assessment, and OCT-based vibrometry has the potential to bridge the gap between structural visualization and mechanical function (Kim et al., 2024; Liu et al., 2025; Park et al., 2018). Nevertheless, translating OCT vibrometry into routine research or clinical use faces several technical and interpretational challenges. High-resolution volumetric acquisitions produce large datasets that require dedicated processing pipelines (Liu et al., 2024). The translucent TM yields low backscatter, and mechanical and environmental motion introduce phase noise and motion artefacts that elevate the measurement noise floor. In ex-vivo studies, dehydration of middle-ear tissues causes rapid stiffening and can bias frequency responses (Gladiné and Dirckx, 2019; Livens et al., 2021; Rosowski et al., 1990). Therefore, these issues create a need for efficient data-collection that delivers both high spatial and high frequency density to maximize diagnostic value.

To address these limitations, we introduce a multisine based OCT vibrometry technique as an efficient, frequency-dense approach for measuring TM mechanics in a single volumetric acquisition. By stimulating the TM with phase and amplitude optimized multisine waveforms, the method simultaneously probes a selected range of acoustic frequencies, enabling rapid capture of the TM's response without repeated single-frequency scans. The multisine approach allows inspection of the motion at the umbo for all input frequencies and enables visualization of the vibration surface across the TM for a single frequency. Compared to a tone-sweep, the multisine is advantageous because it allows a better choice of stimulation frequency and bandwidth, thus enabling a higher signal-to-noise ratio. This approach improves sensitivity to lesion-specific signatures: changes in the resonance at the umbo provide an indication of TM pathology, such as perforation and ablation, while the displacement surfaces pinpoint the pathologies' location, especially at high frequencies. To our knowledge, only one previous study has applied multisine excitation in the context of OCT vibrometry (Lui et al., 2021). However, the focus was on the feasibility of their hand-held OCT setup, and not the diagnostic value of multisine stimulation.

In this paper we demonstrate the feasibility and diagnostic promise of multisine OCT vibrometry as a diagnostic tool for middle ear pathologies using a New Zealand white rabbit model. We quantify the method's sensitivity, compare control and lesioned (ablated and perforated) TMs, and show that lesion type produces distinct frequency-dependent and spatially localized responses. Our results indicate that multisine OCT vibrometry can distinguish pathological from healthy ears and discriminate between different classes of TM damage.

Materials & Methods

Sample preparation

Six fresh-frozen rabbit heads were obtained from a local breeder (Peeters – Verbaeten, Ranst, Belgium). From these twelve ears, three ears were omitted from the measurements due to damage or a large degree of effusion in the ear canal. Two samples were used for testing different stimulation protocols and sound levels. Data on the seven remaining ears was obtained on the same day with the same experimental protocol. The samples were prepared at the Bio- & Medical research lab, Antwerp, Belgium, following previously reported guidelines (Livens et al., 2021; Livens and Dirckx, 2023a, 2023b). The heads were slowly defrosted and wrapped in moist paper to avoid dehydration. Then, the tympanic bulla, containing the ear canal, middle ear cavity and the inner ear was removed from the head. Next, the ear canal was removed to allow for visual access to the TM. In Fig. 1A, a prepared rabbit eardrum is shown. Following Burkhardt et al. (2014), we chose to acoustically stimulate the eardrum medially via an opening in the middle ear cavity. We made an opening of approx. 2 mm in the middle ear cavity using a surgical drill, as shown in Fig. 2B. Then, a 3D printed connector for the microphone and speaker was positioned and securely sealed using two component silicone paste (Dreve Otoplastik, Otoform Ak X), as shown in Fig. 1C. After preparation, each sample was wrapped in wet paper and frozen. Samples were then transported to the Applied Optics Group at the University of Kent, Canterbury, UK to perform OCT measurements.

We prepared five samples to serve as a control group. These samples will be denoted by S1 to S5 onwards. S1, S4, and S5 were left ears, while S2 and S3 were right ears, respectively. Two samples were prepared and deliberately lesioned to serve as a pathological group. For sample S6 (a left ear), we partially ablated the lateral eardrum surface using a 0.8 mm drill (Dremel, Nr. 105). In Fig. 1D, the location of ablation is highlighted in green. The inset provides a larger view of the ablated, but not perforated, eardrum. For sample S7 (a left ear), we deliberately punctured the eardrum using a 0.6 mm needle (Terumo, Nr. 23G), as shown in Fig. 1E.

Multisine sound stimulation

To efficiently collect data using a single OCT-vibrometry volume, sound stimulation was done via multisine tones (Gladiné, 2019; Peacock et al., 2015; Wales et al., 2025). The input pressure $P(t)$ of pressure amplitude p is defined as a linear combination of K components with frequencies ν_i and phases γ_i, respectively

$$P(t) = \frac{p}{\sqrt{K}} \sum_{i=1}^{K} \sin(2\pi\nu_i + \gamma_i) \qquad (1)$$

Normalization by $\sqrt{K}$ guarantees that the total sound intensity level stays the same irrespective of the number of frequencies selected to construct $P(t)$. The sound's phase γ_i is determined by minimization of the so-called crest factor using Matlab's *fminsearch* (Grauer, 2022; Michael, 2012; Morelli, 2021). In doing so, large peak amplitudes in the signal $P(t)$ are avoided.

After calibration of the sound's phase, a second procedure was used to normalize the amplitude for each frequency. A multisine tone with equal input amplitude voltages across frequencies was sensed by the earbud (Sennheiser CX 300 II). Because of the earbud's frequency response, this did not produce a flat acoustic spectrum. The acoustic spectrum was therefore measured with a calibration microphone (Brüel & Kjær, type 4182), and the input was adjusted iteratively until the sound pressure level at each frequency was within 1 dB of the target amplitude $p/\sqrt{K}$.

Equation (1) allows for an arbitrary number of frequencies. However, a balance must be found between frequency density and the ability to resolve individual displacements.

To achieve a good signal-to-noise without introducing nonlinearities in the displacements, a pressure level of 100 dB SPL (i.e., 2 Pa) was used (Aerts and Dirckx, 2010; Peacock et al., 2015). Frequency signals from 800 to 6000 Hz, with a step of 200 Hz, were generated. Therefore, the multisine signal used in this study had 27 frequency components with a pressure level of 0.38 Pa each. We verified that the current choice of multisine stimulation exceeded the noise floor of our setup (additional details are presented in Results section).

Note that using multisine stimulation, interpreting and analyzing phase information is more involved. The phase term γ_{i} mitigates large peaks of the input pressure signal. When analyzing the phase of the *displacement*, one must subtract the phase term γ_{i} from each frequency component ν_i. Since our results showed identifiable changes in displacement amplitude due to ablation or perforation, we present only data on changes in the displacement amplitude in the present work.

OCT vibrometry

A custom spectral domain OCT-vibrometry setup was developed to allow for capturing the TMs motion under multisine stimulation. Displacement of scatterers within a medium will cause changes in the phase of the OCT signal. The phase difference $\Delta\Phi\,(\mathrm{t})$ between consecutive A-scans can be related to the displacement of the scatterer $\Delta\mathrm{z}\,(\mathrm{t})$ as (Drexler and Fujimoto, 2015; Hendargo et al., 2011; Wang and Nuttall, 2010)

$$\Delta\mathrm{z}\,(\mathrm{t}) = \frac{\lambda_c}{4\pi}\Delta\Phi\,(\mathrm{t}) \tag{2}$$

In the equation above, λ_c denotes the central wavelength of the optical setup. When the input stimulus is a multisine, the phase $\Delta\Phi_{multisine}\,(\mathrm{t})$ can be expressed as

$$\Delta\Phi_{multisine}\,(\mathrm{t}) = \sum_{i=1}^{K} A_i \sin\left(2\pi\nu_{\mathrm{i}} + \theta_{\mathrm{i}}\right) + \varphi_i \tag{3}$$

with θ_{i} the phase of the displacement w.r.t the sound pressure. The random phase noise φ_{i} defines the noise floor of the measurement for each frequency component. Since we have constructed and calibrated an equally weighted stimulation pressure signal, see Eq. (1), the displacement amplitudes A_i characterizes the ME's frequency response.

Our OCT setup was developed at the Applied Optics Group, following a spectral domain approach (Bradu et al., 2015; Park et al., 2018). A superluminescent diode source with a

central wavelength of 840 nm and a 50 nm spectral bandwidth (Superlum Broadlighter, model S840) was used. The resulting axial resolution, experimentally measured in biological tissue, was 5 μm. The displacement resolution is frequency and location depended, see Results for more information. In the sample arm, two orthogonal galvanometer mirrors (Thorlabs, GVS002) scanned the optical beam across the sample, which was focused by a 54 mm focal length scan lens (Thorlabs, LSM04-BB). Light backscattered from the sample was recombined with reference arm light and detected by a custom-built spectrometer. The spectrometer included a 1,200 lpm transmission diffraction grating (Wasatch Photonics) that dispersed the spectrum onto a fast line-scan camera (Teledyne e2v, Octoplus USB). Galvanometer positioning and line-camera triggering were controlled via a multifunction I/O device (National Instruments, PCIe-6321) and custom LabVIEW software. The acquisition rate of the camera was 100 kHz, yielding one A-scan profile every 10 μs. Complex OCT images were generated using the Master–Slave method (Bradu et al., 2018) and displayed in real time.

Each vibrometry B-scan consisted of 130 lateral, 200 axial, and 500 temporal samples. To cover the measurement volume, 50 B-scans were acquired, providing a balance between scan duration, data size, and spatial resolution. The total acquisition time was 5 minutes. The resulting voxel sizes in the X, Y, and Z dimensions were 89, 224, and 5 μm, respectively. OCT intensity and phase data were saved as binary files for subsequent processing. The resulting intensity volume was loaded into segmentation software (Dragonfly 3D, V2024.1). Using Otsu thresholding and manual outlier removal, a mask was created separating the relevant voxels from background. Using Eq. (3), the differentiated phase data $\Delta\Phi_{multisine}(t)$ was used in MATLAB to compute the displacement amplitude via the Fourier transform.

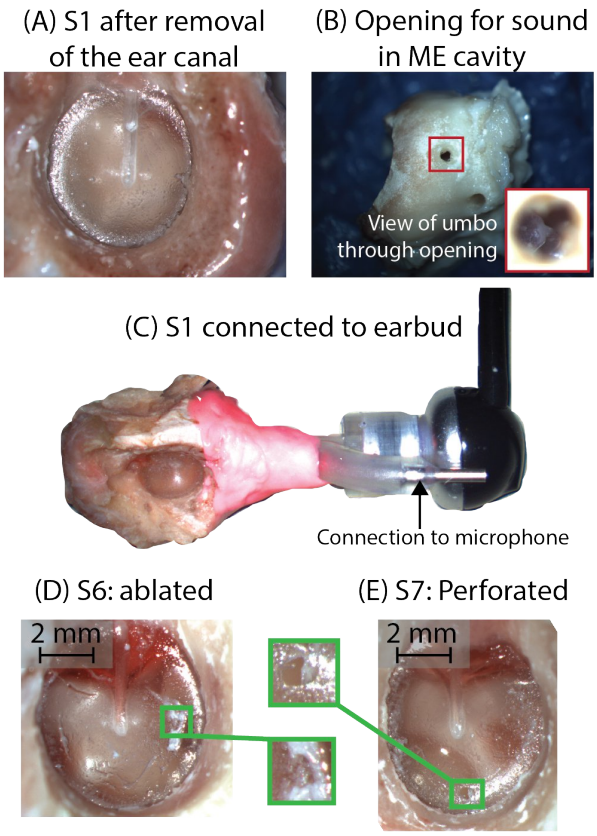

Fig. 1 *The ear canal is removed to allow for visual access to the TM (A). An opening is made in the ME cavity to stimulate the TM medially (B). A 3D printed connector is then positioned (C). Two samples are created to investigate pathological TMs. S6 is ablated, but not perforated (D), and S7 has been punctured (E).*

Results

Noise floor characterization

We first sought to characterize the noise floor of our multisine OCT-vibrometry system. The displacement noise floor arises from random phase noise φ_i, as in Eq. (3), which can originate from several sources, including phase jitter in the superluminescent diode, mechanical vibrations of the setup, and low backscatter intensity leading to poor signal-to-noise ratios (SNR). This problem is particularly pronounced in the translucent eardrum, where voxel intensity is often low, reducing the phase SNR of individual A-scans and thereby elevating the displacement noise floor.

To evaluate the noise floor level, we acquired an OCT-vibrometry volume with the earbud switched off and processed the data as described in *Materials & Methods*. The resulting displacement amplitudes then characterizes the sensitivity of our setup, as shown in Fig. 2A (logarithmic scale). The malleus is outlined in white to aid orientation. These data reflect the cumulative error of the entire processing pipeline and provides a spatially

dependent noise floor estimate. Overall, the displacement error typically ranges from 1–2 nm, but certain data points exceed 10 nm.

To improve data interpretability and visualization, we generated a mesh representing the mid-layer of the tympanic membrane (TM). The mesh was constructed from the average Z-location of each column in the volume and discretized into triangular elements with ~200 μm edges. For each mesh node, displacement values were averaged using Gaussian weighting with window size σ. Figure 2B shows the result for $\sigma = 10^{-0.8}$ mm (≈160 μm). Data averaging reduced the noise floor to <1 nm across the eardrum, though higher errors of 2 nm remain on the anterior and posterior TM surface near the malleus, likely due to fewer voxels available for averaging in these slanted regions.

Evidently, the choice of window size σ directly influences the degree of data filtering. A range of σ values were tested, and for each we plotted the displacement distribution over the entire mesh as boxplots (Fig. 2C, left axis). As σ increased, averaging reduced both the mean displacement and interquartile range. However, the median and median absolute deviation (MAD) are more robust estimators of the overall displacement noise floor and noise floor displacement spread, respectively (Rousseeuw, 1991; Rousseeuw and Hubert, 2017). Therefore, we looked at the ratio of median to MAD to objectively set σ (Fig. 2C, right axis). In essence, the median to MAD ratio tells us how the distribution of the noise floor data changes due to increasing σ. As seen in Fig. 2C the median to MAD ratio is stable over a range of σ values but increased sharply for $\sigma > 10^{-0.8}$ mm, where the data became over smoothed. Based on this criterion, we selected $\sigma = 10^{-0.8}$ mm for all subsequent analyses.

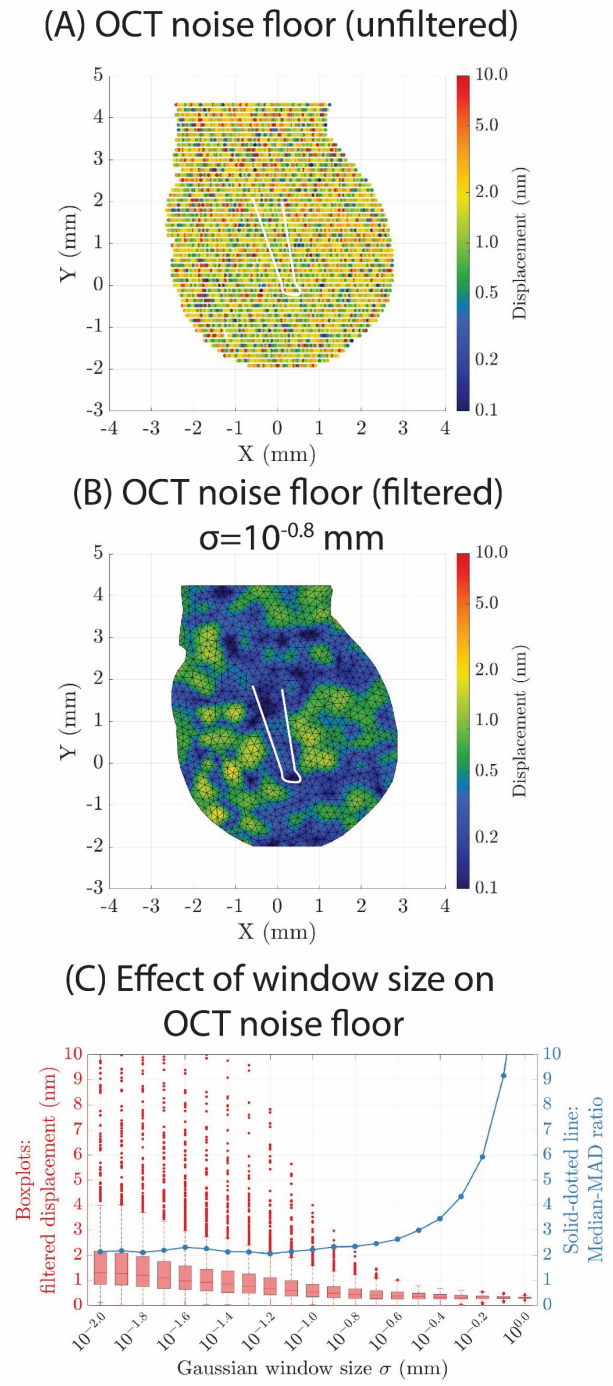

Fig. 2 *Displacement noise floor map obtained from OCT-vibrometry without an input sound (A). Displacement data are shown on a logarithmic scale; the malleus is outlined in white. Typical errors are 1–2 nm, with some regions exceeding 10 nm. Averaging with a window of* $\sigma = 10^{-0.8}$ *mm lowers the noise floor to <1 nm across most of the TM, with higher errors near the anterior and posterior regions adjacent to the malleus (B). Increasing the window size σ leads to decreased interquartile ranges when plotting all data as a boxplot (C, left axis). The ratio between the median and median absolute deviation (MAD) is a robust estimate of the underlying distribution. The ratio is stable over a wide range (2C, right axis). However, it increased for* $\sigma > 10^{-0.8}$ *mm, so this values balances noise filtering and introducing bias optimally.*

Measured umbo displacement

To analyze the umbo displacement of our eardrums, we 1) segmented the OCT volumes to delimitate the TM from the surrounding tissue, 2) computed a custom triangular mesh of the TM shape with ~200 μm edges, and 3) filtered the data using Gaussian weighting ($\sigma = 10^{-0.8}$ mm). Then, we selected the node at the apex of the TM to inspect the displacement amplitude for all TMs. The results for all control eardrums, as the noise floor dataset, are shown in Fig. 3A. The multisine signal identified a resonance around 1.2-1.4 kHz for the individual ears, with a displacement amplitude between 80 to 100 nm. Only for S2 a lower displacement amplitude of 40 nm was found.

To compare the lesioned eardrums (S6 and S7) with the control group, we first computed the control average. For each frequency, we computed the weighted mean displacement using the mean displacements and corresponding standard deviations of Fig. 3A. The result is shown by the solid-circle line in Fig 3B. The average response curve shows that the umbo's displacement is maximal at 1.4 kHz with an amplitude of 86 ± 11 nm, and a decrease in displacement amplitude for increasing stimulation frequencies.

The partially ablated sample S6 is shown as a purple solid-triangular line in Fig. 3B. For S6, the displacement at 1.4 kHz is similar in amplitude to that of the control mean, but maximal displacement is reached at 1 kHz, with a value of 84 ± 4 nm, for S6. At 1.6 kHz, we see a clear drop in displacement amplitude, in contrast with the control group. For higher frequencies the displacement of the control mean and S6 are similar. For S7, the fuchsia solid-square line in Fig. 3B, we see that the frequency of maximal displacement has shifted to 2 kHz. However, the displacement amplitude is very similar to that of the control group at 2 kHz. For frequencies above 2 kHz, the displacement amplitude is very similar to the control. In contrast to S6, we see that the displacement amplitude below 1.2 kHz is lower than the average for S7.

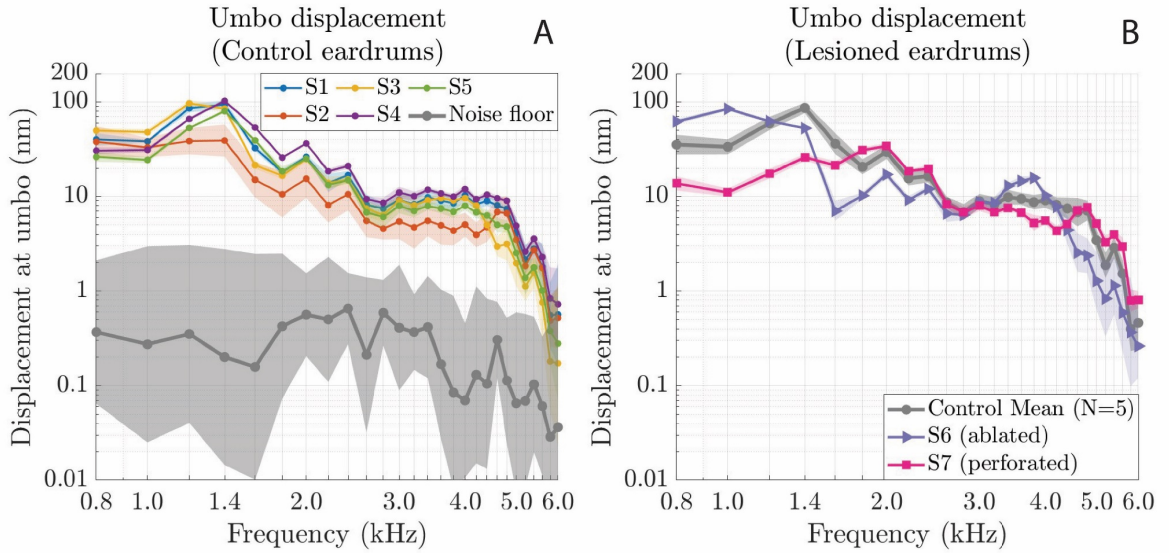

Fig. 3 Average d*isplacement at the umbo measured using multisine OCT vibrometry (A). Data are the result of Gaussian averaging using a window of 160 µm. Five control ears have been measured, showing similar displacement curves. The noise floor data is also shown. These individual curves are averaged to get the mean displacement of the control group at the umbo (B, grey solid-circle line). In S6 (purple solid-triangle line), the partial ablation causes a shift to a lower resonance frequency of 1 kHz, and a sharp drop in displacement at 1.6 kHz. For S7 (pink solid-square line), the perforation causes a shift of the resonance to 2 kHz and a relatively low resonance amplitude.*

Displacement maps of control vs. lesioned ears

As a final exploration of our results, we plotted the displacement across the TM's surface for a selection of frequencies, as shown in Fig. 4. Figures 4A-4C illustrate the displacement maps of S1 at 1400 Hz, 4000 Hz, and 5400 Hz, respectively. Although the displacement amplitude changes with increasing frequency, the overall displacement surface stays similar. For S2, a similar observation can be made in Figs. 4D-F.

In contrast, the lesioned TMs show different displacement maps when comparing different stimulation frequencies. In Figs. 4G-I, the results for S6 are shown. The location of partial ablation is highlighted via the white dashed circle. At 1400 Hz, Fig. 4G, the vibration pattern is very similar to that of Figs. 4A and 4D. At 4000 Hz, Fig. 4H, we observe a distinct lobe appearing on the displacement maps at the location of ablation. At 5400 Hz, Fig. 4I, a high amplitude displacement zone is seen at the location of ablation, and the surrounding parts of the TM surface displace much less.

The results for S7 are shown in Figs. 4J-4L. The perforation is seen as a hole at the inferior part of the TM surface, since no OCT data is present at that location. For a frequency of 1400 Hz, Fig. 4J, the displacement surface is similar to that of the control TMs. At a frequency of 4000 Hz, Fig. 4K, we see that the displacement amplitude around the hole is around 10 nm, similar to the displacement amplitudes seen in the posterior part of the TM. At a frequency of 5400 Hz, Fig. 4L, the TM moves the most around the perforation with amplitude around 9 nm, and there is a secondary lobe of high displacement amplitude slightly more anterior-superior with respect to the hole. The effect of the

perforation seems quite localized, since the posterior zone of S7, Fig. 4L, moves with an amplitude around 7 nm, which is comparable to the control ears at 5400 Hz, Figs. 4C and 4F. Overall, we observe that the lesions cause localized effects on the TMs vibration surfaces.

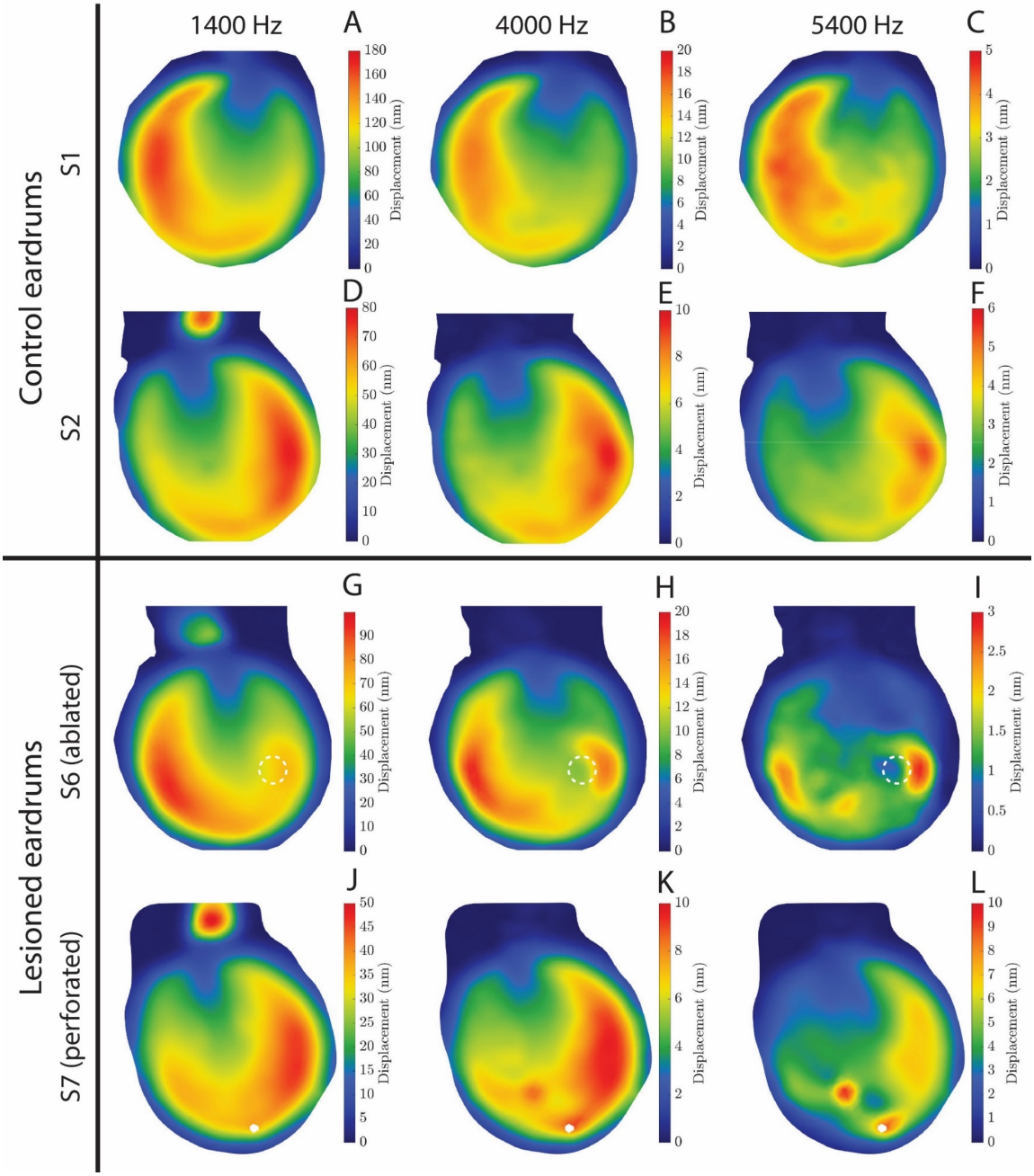

Fig. 4 *Displacement of control eardrum S1 at 1400 Hz (A), 4000 Hz (B), and 5400 Hz (C). Most of the displacement is seen in the posterior quadrant. Control eardrum S2 has similar behavior at 1400 Hz (E), 4000 Hz (F), and 5400 Hz (G). For the ablated eardrum S6, we see that increasing the stimulation frequency from 1400 Hz (G) to 4000 Hz (H), and finally 5400 Hz (I) introduces a localized displacement pattern around the ablation (dashed circle). For S7 (perforated) the effect at frequencies 1400 Hz (J), 4000 Hz (K), and 5400 Hz (L) is more localized, and the overall displacement pattern is similar to the control ears.*

Discussion

This paper explored multisine OCT vibrometry to characterize the vibrational response of the eardrum. Since human material is limited, we used the New Zealand white rabbit as an animal model. We showed on five control ears that the multisine stimulation allowed efficient capture of the frequency response based on a single OCT-vibrometry volume. The average displacement at the umbo was maximal for a stimulation frequency of 1.4 kHz and had an amplitude of 86 ± 11 nm. For S6, which was ablated, but not perforated, we found the umbo displacement was maximal at 1 kHz, with an amplitude of 84 ± 4 nm. For S7, which was perforated, the maximal displacement was 34 ± 3 nm at a frequency of 2 kHz.

Therefore, multisine stimulation allows comparing the frequency-displacement curve at the umbo with an average control curve to discern between healthy and pathological ears. Moreover, our setup allowed capturing the displacement of the eardrum surface. We showed that the lesioned TMs had distinct vibration patterns compared to the control eardrums, again highlighting the benefit of frequency dense data collecting using multisine stimulation. However, multisine stimulation makes interpreting phase information more difficult. Since creation of the multisine tone requires tuning of the phase term γ_i, one needs to subtract this phase delay from the displacement signal. Figure 3B showed that the ablated sample S6 reached maximal displacement at 1 kHz. The data at 0.8 and 1.2 kHz also shows large displacement amplitudes, and without phase info the relative timings between these frequency components is unknown. If phase data are essential, we suggest collecting multisine data, and then selecting targeted frequencies to repeat the measurements on using pure tones.

Comparing our displacement data to literature, we found some key differences. For example, Peacock et al. (2015) measured umbo vibrations of the rabbit umbo using Laser Doppler Vibrometer (LDV) and a multisine tone stimulus. A resonance peak at 1.8 kHz is reported (their Fig. 5B). After converting their 90 dB SPL (26 frequencies) multisine to the 100 dB SPL (27 frequencies) of the current study, an amplitude around 80 nm is found. Recent studies using the rabbit as an animal model have highlighted the rapid onset of dehydration artefacts when opening the bulla (Gladiné and Dirckx, 2019; Livens et al., 2021; Livens and Dirckx, 2023b). Therefore, the higher resonance frequency reported by Peacock et al. (2015) compared to our data may be the result of dehydration effects, since fully opened bulla were used.

The effect of dehydration on umbo displacement is also found elsewhere in literature. For example, Salih et al. (2016) measured rabbit umbo displacement using X-ray stereoscopy, while Gladiné and Dirckx (2019) used digital image correlation (DIC). Both applied linear pressure cycles of ± 2 kPa presented to the rabbit's lateral TM surface. Salih et al. (2016) partially opened the bulla to place tungsten beads at the umbo for motion tracking and closed the bulla using wet paper during measurements. In contrast, Gladiné and Dirckx (2019) required optical access for DIC, opened the bulla as much as possible, and subsequently measured with the medial TM surface open to the air. Salih et al. (2016) reported umbo displacements of 211 ± 25 μm, while Gladiné and Dirckx (2019) reported 153 ± 14 μm. These data highlight the importance of keeping the bulla closed to obtain representative umbo displacements. To mitigate dehydration as much as possible, we

measured the eardrum from the lateral side and followed a similar approach as taken by Burkhardt et al. (2014) by stimulating the eardrum medially.

The displacement surfaces of Fig. 4 show a decrease in displacement amplitude with increasing frequency. However, unlike human eardrums, which exhibit complex vibration patterns at higher frequencies (Burkhardt et al., 2014; De Greef et al., 2014), our data show only limited changes in mode shape across the measured frequency range. Chinchilla eardrums display complex mode shapes from 2.5 kHz onwards (Rosowski et al., 2013), but measurements on rabbit eardrums showed complicated displacement surfaces only from 6.4 kHz (De Greef and Dirckx, 2014). This delayed onset of higher-order vibration patterns may, therefore, be a species-specific feature of the rabbit eardrum. Changes in human umbo or stapes displacement due to eardrum perforations are well established (Bevis et al., 2022; Gan et al., 2009; Voss et al., 2001b), so we expect that multisine OCT can be directly used for such purposes. However, future work should focus on how well localized defects in the vibration mode shapes are detectable using pure tone or multisine OCT.

The measurements were performed without access to a surgical microscope. Therefore, we prepared our control and lesioned TMs at the University of Antwerp. Other studies have focused on the effect of TM perforation size and location in human temporal bone samples, and used a pre- and post-perforation comparison (Bevis et al., 2022; Nishihara et al., 1993; O'Connor et al., 2008; Voss et al., 2001a, 2001b). Since our goal was to investigate whether the multisine stimulation allowed discerning between the two groups, and not the precise effect of the lesion, we found this sufficient for the current study. Given that Figs. 3 and 4 show that multisine OCT vibrometry allows discerning between control and pathological ears, a follow up study on the precise changes between pre- and post-lesion could provide valuable insight into the effects of perforation size and location on TM vibrational modes.

One important consideration for clinal translation is the available field-of-view (FOV). In this study, we removed the ear canal to enable measurements across the entire TM surface. In a clinical setting, however, the available FOV will be much more limited. Nevertheless, we showed that multisine stimulation allows detecting of ablation or perforation induced frequency shifts at the umbo, see Fig. 3B. Therefore, measurements with limited FOV show diagnostic potential provided the umbo is included in the OCT volume.

The effect of eardrum perforation in our rabbit data (S7) is similar to that found in human MEs: a drop in displacement amplitude at low frequencies, and less pronounced differences at high frequencies (Bevis et al., 2022; Nishihara et al., 1993; Voss et al., 2001a; Zhang et al., 2012). For example, Voss et al. (2001a) reported a decrease of 10 dB in stapes velocity with a 0.5 mm perforation. In rat, a perforation of 20% of the total TM area caused a 10 dB drop in umbo velocity, but little change was observed for a 4% perforation (Bigelow et al., 1996). Therefore, using single-point data at the umbo, lower stimulation frequencies seem better suited to detect TM perforation. However, comparing the displacement surfaces of Figs. 4C and 4L with 4F shows that perforations significantly alter the surface motion at high frequencies, but that the effect is quite localized. Moreover, the location of a perforation is visible immediately via the hole in the mesh.

Multisine OCT vibrometry could thus allow for robust detection of TM perforations by first looking at low frequency single point measurements at the umbo, followed by inspection of the high frequency displacement surfaces.

For S6 (ablated but not perforated), we observed an effect opposite to the perforation: an increase in displacement amplitude at low frequencies compared to the control, followed by a significant drop at 1.6 kHz, see Fig. 2B. Nishihara et al. (1993) explored the effect of removing the epithelium of the entire pars tensa surface using LDV. They found a slight decrease in umbo displacement between 0.3-1 kHz, and an increase above 1 kHz, i.e., opposite to our observations. To the best of the authors' knowledge, no papers describe the effect of local partial ablation on the TM's displacement response. However, the effect of locally adding mass has been explored. Nishihara et al. (1993) loaded the posterior TM surface using clay spheres ranging from 0.5 mm to 2 mm in diameter. They report a decrease in umbo displacement between 0. 15-1 kHz, an increase from 1-2 kHz, and rapid changes above 2 kHz (their Figs. 4A-B). Aarnisalo et al. (2010) placed 6 mm by 3 mm oval cartilage grafts with thicknesses of 0.5 to 1 mm posteriorly on the TMs medial surface. They report an overall decrease in TM motion caused by application of cartilage. While these studies involve mass loading rather than removal, their results support the notion that local changes in mass and stiffness can produce opposite trends in the TM's vibrational response.

The present data thus extend existing findings by highlighting that local thinning substantially reduces the bending stiffness of the membrane, leading to an increase of the umbo's displacement amplitude at low frequencies. Perforations, however, cause a pressure shunt (Bigelow et al., 1996), decreasing the pressure differential between the medial and lateral TM surface, and subsequently decrease the umbo's displacement amplitude across all frequencies.

OCT vibrometry has grown from a fundamental research tool to a promising candidate to be used in clinical practice (Lui et al., 2021; MacDougall et al., 2019). Current limitations are rapid data acquisition to minimize motion artifacts, while maintaining high spatial resolution to support detailed diagnostic assessment. Since middle ear pathologies manifest distinct responses at specific acoustic frequencies (Al-Salim et al., 2024; Gladiné et al., 2018; Rosowski et al., 2011; Wales et al., 2025), multisine excitation presents a promising alternative by enabling accurate broadband assessment. Given the current findings, future work should focus on collecting multisine data of human ME dysfunction such as ME effusion, eardrum ablation or perforation, and otosclerosis. Comparing their distinct frequency cues using multisine OCT would enable robust classification of ME pathologies in a non-invasive manner. Combining the information provided via the umbo displacement curve at low frequencies, with the vibration surfaces at high frequencies, shows great promise as a diagnostic tool. Therefore, this combined approach has the potential to enhance the detection of eardrum pathologies and support more informed surgical decision-making.

Conclusion

This study demonstrates that multisine OCT vibrometry provides an efficient and robust approach for assessing eardrum vibrations across a wide frequency range using a single

OCT volume. A multisine signal was constructed with tones from 0.8 to 6 kHz in steps of 200 HZ, i.e., 27 frequency components were contained in the signal. The total sound pressure level was set to 100 dB SPL for all measurements. Using healthy rabbit eardrums as an animal model, the method captured consistent umbo displacements, showing maximal displacement of 86 ± 11 nm at 1.4 kHz.

In contrast, proof-of-concept measurements on abnormal eardrums showed that the multisine dataset allowed detection of pathology-related frequency changes of the umbo's displacement response. Ablated eardrums showed an *increase* in displacement amplitude at lower frequencies (<1.4 kHz), with a maximal displacement of 84 ± 4 nm at 1 kHz. In contrast, eardrum perforation causes a clear drop in umbo displacement amplitude, with a maximal displacement of 34 ± 3 nm reached at 2 kHz.

These results demonstrate that while umbo displacement curves are sufficient to differentiate healthy from pathological eardrums, surface displacement maps provide additional detail by uncovering lesion-specific vibration patterns. The combination of frequency-dependent and spatially resolved measurements highlights the diagnostic value of multisine OCT vibrometry for distinguishing between different types of tympanic membrane pathologies, with strong potential to inform clinical evaluation and guide surgical decision-making.

Funding sources

P. Livens acknowledges the support of the Research foundation Flanders (FWO) under grant nr. 1273723N. A. Bradu acknowledges the support of the Royal Society, project PARSOCT, RGS/R1/221324, and the support of the Academy of Medical Sciences/the Welcome Trust/the Government Department of Business, Energy and Industrial Strategy/the British Heart Foundation/Diabetes UK Springboard Award SBF007\100162.

Declaration of competing interests

The authors declare that they have no known competing financial interests or personal relationships that could have appeared to influence the work reported in this paper.

References

Aarnisalo, A.A., Cheng, J.T., Ravicz, M.E., Furlong, C., Merchant, S.N., Rosowski, J.J., 2010. Motion of the tympanic membrane after cartilage tympanoplasty determined by stroboscopic holography. Hear Res 263, 78–84. https://doi.org/10.1016/j.heares.2009.11.005

Aerts, J.R.M., Dirckx, J.J.J., 2010. Nonlinearity in eardrum vibration as a function of frequency and sound pressure. Hearing Research, MEMRO 2009: Middle-Ear Science and Technology 263, 26–32. https://doi.org/10.1016/j.heares.2009.12.022

Al-Salim, S., Skretta, D., Merchant, G.R., 2024. Survey of Wideband Acoustic Immittance Use by Clinical Audiologists. Am J Audiol 33, 254–268. https://doi.org/10.1044/2023_AJA-23-00228

Bevis, N., Sackmann, B., Effertz, T., Lauxmann, M., Beutner, D., 2022. The impact of tympanic membrane perforations on middle ear transfer function. Eur Arch Otorhinolaryngol 279, 3399–3406. https://doi.org/10.1007/s00405-021-07078-9

Bigelow, D.C., Swanson, P.B., Saunders, J.C., 1996. The Effect of Tympanic Membrane Perforation Size on Umbo Velocity in the Rat. The Laryngoscope 106, 71–76. https://doi.org/10.1097/00005537-199601000-00014

Bradu, A., Israelsen, N.M., Maria, M., Marques, M.J., Rivet, S., Feuchter, T., Bang, O., Podoleanu, A., 2018. Recovering distance information in spectral domain interferometry. Sci Rep 8. https://doi.org/10.1038/s41598-018-33821-0

Bradu, A., Maria, M., Podoleanu, A.Gh., 2015. Demonstration of tolerance to dispersion of master/slave interferometry. Opt. Express 23, 14148. https://doi.org/10.1364/OE.23.014148

Burkhardt, A., Kirsten, L., Bornitz, M., Zahnert, T., Koch, E., 2014. Investigation of the human tympanic membrane oscillation ex vivo by Doppler optical coherence tomography. Journal of Biophotonics 7, 434–441. https://doi.org/10.1002/jbio.201200186

Chang, E.W., Cheng, J.T., Röösli, C., Kobler, J.B., Rosowski, J.J., Yun, S.H., 2013. Simultaneous 3D imaging of sound-induced motions of the tympanic membrane and middle ear ossicles. Hearing Research 304, 49–56. https://doi.org/10.1016/j.heares.2013.06.006

De Greef, D., Aernouts, J., Aerts, J., Cheng, J.T., Horwitz, R., Rosowski, J.J., Dirckx, J.J.J., 2014. Viscoelastic properties of the human tympanic membrane studied with stroboscopic holography and finite element modeling. Hearing Research 312, 69–80. https://doi.org/10.1016/j.heares.2014.03.002

De Greef, D., Dirckx, J.J.J., 2014. Measurement of rabbit eardrum vibration through stroboscopic digital holography. AIP Conference Proceedings 1600, 323–329. https://doi.org/10.1063/1.4879598

Drexler, W., Fujimoto, J.G. (Eds.), 2015. Optical Coherence Tomography: Technology and Applications. Springer International Publishing, Cham. https://doi.org/10.1007/978-3-319-06419-2

Gan, R.Z., Cheng, T., Dai, C., Yang, F., Wood, M.W., 2009. Finite element modeling of sound transmission with perforations of tympanic membrane. J Acoust Soc Am 126, 243–253. https://doi.org/10.1121/1.3129129

Gladiné, K., 2019. Mechanics of the middle ear: Optical measurements and finite-element modeling. Antwerp.

Gladiné, K., Dirckx, J.J.J., 2019. Strain distribution in rabbit eardrums under static pressure. Hearing Research 381, 107772. https://doi.org/10.1016/j.heares.2019.107772

Gladiné, K., Muyshondt, P., Greef, D.D., Dirckx, J., 2018. Effect of Malleus Handle Fracture on Middle Ear Sound Transmission: Laser Doppler Vibrometry Measurements and Finite Element Simulations, in: The 18th International Conference on Experimental Mechanics. Presented at the The International Conference on Experimental Mechanics, MDPI, p. 516. https://doi.org/10.3390/ICEM18-05423

Grauer, J.A., 2022. Frequency Response Estimation for Multiple Aircraft Control Loops Using Orthogonal Phase-Optimized Multisine Inputs. Processes 10, 619. https://doi.org/10.3390/pr10040619

Hendargo, H.C., McNabb, R.P., Dhalla, A.-H., Shepherd, N., Izatt, J.A., 2011. Doppler velocity detection limitations in spectrometer-based versus swept-source optical coherence tomography. Biomed. Opt. Express 2, 2175. https://doi.org/10.1364/BOE.2.002175

Kim, W., Long, R., Yang, Z., Oghalai, J.S., Applegate, B.E., 2024. Optical coherence tomography otoscope for imaging of tympanic membrane and middle ear pathology. J. Biomed. Opt. 29. https://doi.org/10.1117/1.jbo.29.8.086005

Liu, P., Steuer, S., Golde, J., Morgenstern, J., Hu, Y., Schieffer, C., Ossmann, S., Kirsten, L., Bodenstedt, S., Pfeiffer, M., Speidel, S., Koch, E., Neudert, M., 2024. The Dresden in vivo OCT dataset for automatic middle ear segmentation. Sci Data 11, 242. https://doi.org/10.1038/s41597-024-03000-0

Liu, S., Meng, X., Wang, C., Ma, J., Fan, F., Zhu, J., 2025. Handheld optical coherence tomography for tissue imaging: current design and medical applications. Applied Spectroscopy Reviews 60, 292–316. https://doi.org/10.1080/05704928.2024.2401384

Livens, P., Dirckx, J.J.J., 2023a. Rabbit tympanic membrane thickness distribution obtained via optical coherence tomography. Hearing Research 429, 108701. https://doi.org/10.1016/j.heares.2023.108701

Livens, P., Dirckx, J.J.J., 2023b. Prestrain in the eardrum investigated using laser-ablation perforation: A proof of principle study on the New Zealand white rabbit. Hearing Research 437, 108840. https://doi.org/10.1016/j.heares.2023.108840

Livens, P., Muyshondt, P.G.G., Dirckx, J.J.J., 2021. Prestrain in the rabbit eardrum measured by digital image correlation and micro-incisions. Hearing Research 412, 108392. https://doi.org/10.1016/j.heares.2021.108392

Lui, C.G., Kim, W., Dewey, J.B., Macías-Escrivá, F.D., Ratnayake, K., Oghalai, J.S., Applegate, B.E., 2021. In vivo functional imaging of the human middle ear with a hand-held optical coherence tomography device. Biomed. Opt. Express, BOE 12, 5196–5213. https://doi.org/10.1364/BOE.430935

MacDougall, D., Morrison, L., Morrison, C., Morris, D.P., Bance, M., Adamson, R.B.A., 2019. Optical Coherence Tomography Doppler Vibrometry Measurement of Stapes Vibration in Patients With Stapes Fixation and Normal Controls. Otology & Neurotology 40, e349–e355. https://doi.org/10.1097/mao.0000000000002193

Michael, S., 2012. Multisine Excitation Design to Increase the Efficiency of System Identification Signal Generation and Analysis.pdf.

Morelli, E.A., 2021. Practical Aspects of Multiple-Input Design for Aircraft System Identification Flight Tests.

Nishihara, S., Aritomo, H., Goode, R.L., 1993. Effect of changes in mass on middle ear function. Otolaryngol.--head neck surg. 109, 899–910. https://doi.org/10.1177/019459989310900520

O'Connor, K.N., Tam, M., Blevins, N.H., Puria, S., 2008. Tympanic Membrane Collagen Fibers: A Key to High-Frequency Sound Conduction. The Laryngoscope 118, 483–490. https://doi.org/10.1097/MLG.0b013e31815b0d9f

Park, K., Cho, N.H., Jeon, M., Lee, S.H., Jang, J.H., Boppart, S.A., Jung, W., Kim, J., 2018. Optical assessment of the in vivo tympanic membrane status using a handheld optical coherence tomography-based otoscope. Acta Otolaryngol 138, 367–374. https://doi.org/10.1080/00016489.2017.1395515

Peacock, J., Pintelon, R., Dirckx, J., 2015. Nonlinear Vibration Response Measured at Umbo and Stapes in the Rabbit Middle ear. J Assoc Res Otolaryngol 16, 569–580. https://doi.org/10.1007/s10162-015-0535-7

Ramier, A., Cheng, J.T., Ravicz, M.E., Rosowski, J.J., Yun, S.-H., 2018. Mapping the phase and amplitude of ossicular chain motion using sound-synchronous optical coherence vibrography. Biomed. Opt. Express 9, 5489. https://doi.org/10.1364/BOE.9.005489

Rosowski, J., Cheng, J., Merchant, S., Harrington, E., Furlong, C., 2011. New Data on the Motion of the Normal and Reconstructed Tympanic Membrane. Otol Neurotol 32, 1559–1567. https://doi.org/10.1097/MAO.0b013e31822e94f3

Rosowski, J.J., Davis, P.J., Donahue, K.M., Merchant, S.N., Coltrera, M.D., 1990. Cadaver Middle Ears as Models for Living Ears: Comparisons of Middle Ear Input Immittance. Ann Otol Rhinol Laryngol 99, 403–412. https://doi.org/10.1177/000348949009900515

Rosowski, J.J., Dobrev, I., Khaleghi, M., Lu, W., Cheng, J.T., Harrington, E., Furlong, C., 2013. Measurements of three-dimensional shape and sound-induced motion of the chinchilla tympanic membrane. Hearing Research, MEMRO 2012 – Middle-Ear Bridge between Science and Otology 301, 44–52. https://doi.org/10.1016/j.heares.2012.11.022

Rousseeuw, P.J., 1991. Tutorial to robust statistics. Journal of Chemometrics 5, 1–20. https://doi.org/10.1002/cem.1180050103

Rousseeuw, P.J., Hubert, M., 2017. Computation of Robust Statistics: Depth, Median, and Related Measures, in: Handbook of Discrete and Computational Geometry. Chapman and Hall/CRC.

Salih, W.H.M., Soons, J.A.M., Dirckx, J.J.J., 2016. 3D displacement of the middle ear ossicles in the quasi-static pressure regime using new X-ray stereoscopy technique. Hearing Research, MEMRO 2015 – Basic Science meets Clinical Otology 340, 60–68. https://doi.org/10.1016/j.heares.2015.12.003

Sanford, C.A., Brockett, J.E., Aithal, V., AlMakadma, H., 2023. Implementation of Wideband Acoustic Immittance in Clinical Practice: Relationships among Audiologic and Otologic Findings. Semin Hear 44, 065–083. https://doi.org/10.1055/s-0043-1763295

Voss, S.E., Rosowski, J.J., Merchant, S.N., Peake, W.T., 2001a. How do tympanic-membrane perforations affect human middle-ear sound transmission? Acta Otolaryngol 121, 169–173. https://doi.org/10.1080/000164801300043343

Voss, S.E., Rosowski, J.J., Merchant, S.N., Peake, W.T., 2001b. Middle-ear function with tympanic-membrane perforations. I. Measurements and mechanisms. The Journal of the Acoustical Society of America 110, 1432–1444. https://doi.org/10.1121/1.1394195

Wales, J., Muyshondt, P.G.G., Silvola, J., Livens, P., Gladiné, K., Dirckx, J., von Unge, M., 2025. Minimally invasive intraoperative laser vibrometry (MIVIB) – a peroperative method to measure fixation of the ossicular chain. Laryngoscope Investigative Otolaryngology.

Wang, R.K., Nuttall, A.L., 2010. Phase-sensitive optical coherence tomography imaging of the tissue motion within the organ of Corti at a subnanometer scale: a preliminary study. J Biomed Opt 15, 056005. https://doi.org/10.1117/1.3486543

Zhang, X., Dai, Y., Zhang, S., She, W., Du, X., Shui, X., 2012. Small Tympanic Membrane Perforations in the Inferior Quadrants Do Not Impact the Manubrium Vibration in Guinea Pigs. PLoS ONE 7, e28961. https://doi.org/10.1371/journal.pone.0028961